



# Control of strong electronic oxide-support interaction in iron-based redox catalysts for highly efficient chemical looping CO<sub>2</sub> conversion

Tong Ouyang, Bo Jin<sup>\*</sup>, Yu Mao, Ding Wei, Zhiwu Liang<sup>\*</sup>

Joint International Center for CO<sub>2</sub> Capture and Storage (iCCS), Provincial Hunan Key Laboratory for Cost-effective Utilization of Fossil Fuel Aimed at Reducing Carbon-dioxide Emissions, Advanced Catalytic Engineering Research Center of the Ministry of Education, College of Chemistry and Chemical Engineering, Hunan University, Lu shannan 1, Changsha, Hunan 410082, China

## ARTICLE INFO

### Keywords:

CO<sub>2</sub> conversion  
Chemical looping  
Redox catalyst  
Crystal engineering  
Strong electronic interaction

## ABSTRACT

Moderating oxide/metal-support interactions over redox catalysts is effective way to achieve efficient chemical looping CO<sub>2</sub> conversion, however, identify the interaction type, control the interaction intensity, and reveal its correlation with CO yield from a molecular perspective remain challenging. In this work, a crystal engineering strategy for tuning strong electronic interaction over Fe<sub>2</sub>O<sub>3</sub>/ZrO<sub>2</sub> is reported and demonstrated by theoretical calculations, characterization techniques and reactivity evaluations. Compared to t-ZrO<sub>2</sub>, m-ZrO<sub>2</sub> exhibits a stronger electronic interaction intensity with iron oxide and iron species as well as creates more oxygen vacancy and transfers more electrons to facilitate H<sub>2</sub> and CO<sub>2</sub> activations, which decreases the energy barriers of redox reactions. This mechanism makes Fe<sub>2</sub>O<sub>3</sub>/m-ZrO<sub>2</sub> perform with two times higher of time-averaged CO space time yield (560 mmol<sub>CO</sub>·s<sup>-1</sup>·kg<sub>Fe2O3</sub><sup>-1</sup>) than Fe<sub>2</sub>O<sub>3</sub>/t-ZrO<sub>2</sub>. Electronic interaction intensity shows a positive relationship with CO yield. The findings provide a general guideline to rationally design efficient catalysts for thermochemical and redox reactions.

## 1. Introduction

Anthropogenic CO<sub>2</sub> emissions cause a significant increment of global temperature and raise greenhouse gas effect [1,2]. As one part of carbon capture, utilization and storage (CCUS), CO<sub>2</sub> capture (e.g. amine scrubbing) is an effective route to deal with this environmental issue, but faces with the burden of large energy penalty, high economic cost and potential safety risk [3,4]. If the captured CO<sub>2</sub> can be properly handled, its commercial deployment would be accelerated. Benefitted from the process intensification strategy of coupling reaction and separation, chemical looping CO<sub>2</sub> conversion offers a powerful solution by converting the captured CO<sub>2</sub> into CO as an important building block with an attractive economic compensation [5]. In this process, a redox catalyst (i.e. oxygen carrier or oxygen storage material) involves in the cyclic reduction (MO + reactant → M + product) and oxidation (M + CO<sub>2</sub> → MO + CO) via gas switching or solid looping in a configuration of fixed or fluidized bed reactors [6,7]. Iron-based redox catalyst is singled out as a promising candidate for industrial application due to its high oxygen storage capacity, cheap cost, easily availability and environmental friendliness [8,9], however, it suffers from heavy deactivation during

cycles [10,11].

Tuning the interaction between the support and active iron specie to induce a metal-support interaction (MSI) [12] or an oxide-support interaction (OSI) [13] may be an alternative solution to mitigate the deactivation. Typical MSI/OSI phenomena, consisting of charge transfer [14,15], specific interface [16] and strong metal/oxide-support interaction (SMSI/SOSI) [17], contribute to a profound effect on the performance of catalysts. However, compared to the common strategies of increasing the dispersion of iron species [18,19], designing special morphology [9], altering cation/ion diffusion mechanism [20,21], introducing active metal dopant [22,23], regulating phase composition distribution [24] and using different synthesis protocols [25], the investigation on the control of MSI/OSI over redox catalysts to improve the reactivity is rare and needs more molecular-level understandings on reaction enhancement mechanism. For instance, to elevate the reactivity of Ni-based redox catalysts, the decline of MSI is required to minimize the formation of nickel aluminate [26–28] but a SMSI is generated via in-situ encapsulation of Ni to prevent sintering and create more surface oxygen vacancy [29]. In contrast, a strengthen OSI is benefitted to sintering resistance and decomposition reactivity for Cu-based redox

<sup>\*</sup> Corresponding authors.

E-mail addresses: [kingjinbo1988@hnu.edu.cn](mailto:kingjinbo1988@hnu.edu.cn) (B. Jin), [zwliang@hnu.edu.cn](mailto:zwliang@hnu.edu.cn) (Z. Liang).

<https://doi.org/10.1016/j.apcatb.2023.123531>

Received 6 September 2023; Received in revised form 31 October 2023; Accepted 14 November 2023

Available online 17 November 2023

0926-3373/© 2023 Elsevier B.V. All rights reserved.

catalysts [30]. This indicates that rational tuning the role of MSI/OSI played would remarkably affect the activity and stability of redox catalysts.

For iron-based redox catalysts, the moderation of OSI, the correlation between OSI intensity and redox activity, and the molecular-level interpretation on reaction enhancement mechanism have not yet been investigated, even though the support category and structure contribute to an influence on the OSI. For support types,  $\text{Al}_2\text{O}_3$  reacts with  $\text{Fe}_2\text{O}_3$  to form low active  $\text{FeAl}_2\text{O}_4$  whilst no solid solution is formed for  $\text{ZrO}_2$  and  $\text{MgO}$  [31]. Moreover,  $\text{ZrO}_2$  shows a lower energy barrier but a larger energy barrier than  $\text{Al}_2\text{O}_3$  and  $\text{MgO}$  during the reduction and oxidation of iron oxide, respectively [32]. In terms of support structure,  $\text{LaAl}_2\text{O}_9$  and  $\text{Na-}\beta\text{-Al}_2\text{O}_3$  structures inhibit phase segregation and spinel oxide formation between  $\text{Al}_2\text{O}_3$  and  $\text{Fe}_2\text{O}_3$  [33,34], respectively, while  $\text{Si-O-Al}$  structure suppresses phase transformation ( $\gamma\text{-Al}_2\text{O}_3 \rightarrow \alpha\text{-Al}_2\text{O}_3$ ) and facilitates  $\text{FeAl}_2\text{O}_4$  formation [35]. Despite, as inspired by heterogeneous catalysis, support crystalline phase structure may lead to a different influence on the OSI, which then results in a distinctive performance [13,36]. From the previous studies [37,38], monoclinic zirconia ( $\text{m-ZrO}_2$ ) and tetragonal zirconia ( $\text{t-ZrO}_2$ ) are inferred to play a different role during redox reactions since their distribution and transition exhibit a correlation with activity. Nevertheless, the issues of how  $\text{ZrO}_2$  crystalline phases affect the OSI and reactivity, what kind of OSI govern the reaction, how to control the OSI, and what the relationship between OSI intensity and redox activity are still unclear for iron-based redox catalysts during chemical looping applications.

Herein, in this work, the type, effect, and control of oxide-support interactions between the support and iron oxide are for the first time investigated to achieve efficient chemical looping  $\text{CO}_2$  conversion via a crystal engineering strategy that selecting three  $\text{ZrO}_2$  crystalline phases ( $\text{m-ZrO}_2$ ,  $\text{t-ZrO}_2$ , and their mixtures) as the supports for iron-based redox catalysts. The density functional theory (DFT) calculation is firstly carried out to confirm the type and intensity of OSI between  $\text{ZrO}_2$  and iron oxide. A series of iron-based redox catalysts with varying  $\text{ZrO}_2$  crystalline phases are then synthesized, characterized, and examined to illustrate the difference in physicochemical property and redox reactivity. Detailed characterization techniques and DFT calculations are combined to uncover the control of OSI in iron-based redox catalysts for superior performance and the influence of OSI on the microscopic reaction mechanism. The findings will provide a new interpretation on composition interaction mechanism and establish a novel design strategy for efficient redox catalysts in thermochemical energy conversion and chemical looping processes.

## 2. Experimental section

### 2.1. Synthesis of iron-based redox catalysts

$\text{m-ZrO}_2$  was synthesized by a hydrothermal method [39].  $\text{ZrO}(\text{NO}_3)_2 \cdot x\text{H}_2\text{O}$  (Macklin, 99.5 %) and  $\text{CO}(\text{NH}_2)_2$  (Macklin, 99 %) were firstly dissolved in deionized water under magnetic stirring to form two clear solutions. Then, the solutions were mixed to obtain a milky white  $\text{Zr}^{4+}$  solution with a concentration of  $0.6 \text{ mol} \cdot \text{L}^{-1}$ , which was then transferred to a Teflon-lined stainless-steel autoclave and maintained at  $180^\circ\text{C}$  for 20 h in a blast drying oven. The white product was washed several times with deionized water and ethanol by centrifugation, dried at  $100^\circ\text{C}$  in an oven for 12 h, and calcined at  $400^\circ\text{C}$  for 4 h (temperature ramp rate of  $5^\circ\text{C} \cdot \text{min}^{-1}$ ) to produce the first  $\text{m-ZrO}_2$  material, noted as  $\text{m-ZrO}_{2\_1}$ . Another  $\text{m-ZrO}_2$  sample (namely  $\text{m-ZrO}_{2\_2}$ ) was gained from the direct calcination of  $\text{ZrO}(\text{NO}_3)_2 \cdot x\text{H}_2\text{O}$  (Macklin, 99.5 %) at  $800^\circ\text{C}$  for 4 h.

A co-precipitation method was used to synthesize  $\text{t-ZrO}_2$  [40].  $7.25 \text{ g}$  of  $\text{ZrOCl}_2 \cdot 8 \text{ H}_2\text{O}$  (Aladdin, 99 %) was dissolved in deionized water ( $500 \text{ mL}$ ) and precipitated via adding an excess of ethylenediamine in a dropwise manner. The resulting white turbid solution was refluxed at  $100^\circ\text{C}$  for 24 h. The solid precipitate was washed several times with

deionized water and filtered, dried overnight at  $80^\circ\text{C}$ , and calcined at  $800^\circ\text{C}$  for 4 h (temperature ramp rate of  $5^\circ\text{C} \cdot \text{min}^{-1}$ ) to get the first  $\text{t-ZrO}_2$  material, called  $\text{t-ZrO}_{2\_1}$ . By changing condensation and calcination temperatures into  $80^\circ\text{C}$  and  $650^\circ\text{C}$ , the second tetragonal zirconia sample was formed, marked as  $\text{t-ZrO}_{2\_2}$ .

Zirconia with the mixture of  $\text{m-ZrO}_2$  and  $\text{t-ZrO}_2$  crystal phases was prepared via a glycine combustion protocol using  $\text{ZrO}(\text{NO}_3)_2 \cdot x\text{H}_2\text{O}$  and glycine [40].  $\text{ZrO}(\text{NO}_3)_2 \cdot x\text{H}_2\text{O}$  ( $9.25 \text{ g}$ ) and glycine ( $30 \text{ g}$ ) were dissolved separately in deionized water to obtain clear solutions. The solutions were mixed and stirred magnetically at  $100^\circ\text{C}$  until the mixed solution became a viscous gel. The obtained gel was dried at  $80^\circ\text{C}$  for 48 h, and calcined at  $550^\circ\text{C}$  for 4 h to obtain a sample (temperature ramp rate of  $5^\circ\text{C} \cdot \text{min}^{-1}$ ), labeling as  $\text{mix-ZrO}_{2\_1}$ . As the calcination temperature was adjusted to  $700^\circ\text{C}$ , a new mixed crystal sample was obtained and labeled as  $\text{mix-ZrO}_{2\_2}$ .

Iron-based redox catalysts with different zirconia crystalline types were prepared by a coprecipitation approach [37]. The as-prepared  $\text{ZrO}_2$  sample ( $1.8 \text{ g}$ ) and  $\text{Fe}(\text{NO}_3)_3 \cdot 9 \text{ H}_2\text{O}$  ( $1.01 \text{ g}$ ) were dissolved in deionized water and precipitated by adding ammonia solution in a dropwise way. The red precipitate was dried and calcined at  $700^\circ\text{C}$  (temperature ramp rate of  $5^\circ\text{C} \cdot \text{min}^{-1}$ ) to obtain six iron-based redox catalysts, labeled as  $\text{Fe}_2\text{O}_3/\text{m-ZrO}_{2\_1}$ ,  $\text{Fe}_2\text{O}_3/\text{m-ZrO}_{2\_2}$ ,  $\text{Fe}_2\text{O}_3/\text{t-ZrO}_{2\_1}$ ,  $\text{Fe}_2\text{O}_3/\text{t-ZrO}_{2\_2}$ ,  $\text{Fe}_2\text{O}_3/\text{mix-ZrO}_{2\_1}$ , and  $\text{Fe}_2\text{O}_3/\text{mix-ZrO}_{2\_2}$ .

### 2.2. Material characterizations

The textural property of as-calcined iron-based redox catalysts was measured via  $\text{N}_2$  adsorption-desorption tests at  $-196^\circ\text{C}$  using JW-BK200C instrument. Before the experiment, all the samples were vacuumed at  $130^\circ\text{C}$  for 12 h to remove surface volatile adsorbates. The specific surface area and pore size distribution were determined from five-point Brunauer Emmett Teller (BET) and Barrett-Joyner-Halenda (BJH) methods, respectively. The crystalline phase distribution of freshly and cycled materials was measured by X-ray diffraction (XRD, Bruker D8 ADVANCE) under  $\text{CuK}\alpha$  radiation and the spectra from  $10^\circ$  to  $90^\circ$  was recorded with a constant scanning speed of  $8^\circ \cdot \text{min}^{-1}$ . Gaussian functions and Scherrer formula were adopted to fit the main diffraction peaks and calculate the crystallite size. Inductively coupled plasma optical emission spectroscopy (ICP-OES) was used to analyze the iron loading in the catalysts.

The surface morphology and elemental distribution of catalysts were characterized through scanning electron microscope (SEM), High-resolution transmission electron microscopy (HRTEM) and energy dispersive spectroscopy (EDS). SEM was operated to measure the surface morphology via Hitachi S-4800 detector, while HRTEM and EDS were performed at 200KV using a JEOL JEM-F200 cs-corrected microscope with a Schottky-type field emission gun (FEG). The HRTEM samples were prepared by immersing the lacey carbon film on a copper support grid into the material powder and blowing away excess powder. X-ray photoelectron spectroscopy (XPS) spectra of the samples was recorded on a Thermo-Scientific ESCALAB 250Xi instrument with an  $\text{Al K}\alpha$  X-ray source. The base pressure in the analysis chamber was less than  $2 \times 10^{-7} \text{ Pa}$ . The binding energy was calibrated with reference to  $\text{C1s}$  ( $284.8 \text{ eV}$ ) of amorphous carbon.

$\text{H}_2$  temperature programmed reduction ( $\text{H}_2\text{-TPR}$ ) and  $\text{CO}_2$  temperature programmed oxidation ( $\text{CO}_2\text{-TPO}$ ) were conducted on a chemical adsorption instrument (Micromeritics AutoChem II 2920). Prior to the tests,  $100 \text{ mg}$  sample was taken and placed in a U-shaped quartz tube under a pretreatment procedure of heating up to  $300^\circ\text{C}$  under a He atmosphere ( $60 \text{ mL} \cdot \text{min}^{-1}$ ), keeping the temperature for 1 h and cooling down to room temperature. For  $\text{H}_2\text{-TPR}$ , the pretreated sample was heated from room temperature to  $800^\circ\text{C}$  at a rate of  $20^\circ\text{C} \cdot \text{min}^{-1}$  under  $10\% \text{ H}_2/\text{Ar}$  ( $60 \text{ mL} \cdot \text{min}^{-1}$ ). After the sample was cooled to room temperature,  $\text{CO}_2$  ( $99.99\%$ ,  $60 \text{ mL} \cdot \text{min}^{-1}$ ) was introduced for  $\text{CO}_2\text{-TPO}$  using the same heating conditions as those for  $\text{H}_2\text{-TPR}$ .

## 2.3. Reactivity tests

The oxygen storage capacity, reduction rate and oxidation rate of iron-based redox catalysts were examined on a thermogravimetric analyzer (TGA, STA 2500 Regulus, Netzsch). Typically, the sample was pretreated in a way that heating up to 650 °C at a rate of 20 °C·min<sup>-1</sup> in N<sub>2</sub> (50 mL·min<sup>-1</sup>) for 90 min to remove surface adsorbates and water molecules. After weighting and placing 10 mg samples in an empty crucible, 5 % H<sub>2</sub>/N<sub>2</sub> (50 mL·min<sup>-1</sup>) was injected at 650 °C to complete the reduction half-cycle for 30 min. Then, a CO<sub>2</sub> stream (50 mL·min<sup>-1</sup>, 99.99 %) was introduced and maintained for 30 min to execute an oxidation half-cycle. All the samples were tested for twenty cycles. To assess the redox ability, oxygen storage capacity (R), oxidation rate ( $\theta_{red}$ , mol<sub>[O]</sub>·(s·g<sub>Fe<sub>2</sub>O<sub>3</sub></sub>)<sup>-1</sup>) and reduction rate ( $\theta_{oxi}$ , mol<sub>[O]</sub>·(s·g<sub>Fe<sub>2</sub>O<sub>3</sub></sub>)<sup>-1</sup>) were calculated as below.

$$R = \frac{m_{oxi} - m_{red}}{m_{O_2}} \times 100\%$$

$$\theta_{red} = \frac{|m_{red} - m_{oxi}|}{M_o \times \Delta t \times m_i}$$

$$\theta_{oxi} = \frac{m_{oxi} - m_{red}}{M_o \times \Delta t \times m_i}$$

where,  $m_{O_2}$  is the weight loss by complete reduction of active component in the catalyst,  $m_{oxi}$  and  $m_{red}$  represent the mass of catalysts in the oxidation and reduction half-cycles,  $m_i$  is the mass of Fe<sub>2</sub>O<sub>3</sub> in iron-based catalysts, and  $M_o$  is the relative molar mass of oxygen atoms.

The reactivity of CO<sub>2</sub> conversion to CO was evaluated in a fixed-bed reactor equipped with a stainless-steel tube with an inner diameter of 12 mm. 100 mg sample was placed in the constant temperature zone of the reactor with a quartz wool plug underneath. Two N-type thermocouples were in contact with the inside of the reactor and connected to an electronic furnace to measure and control the reaction temperature. A calibrated gas flow meter was used to maintain the flow rate of inlet gas, while an online infrared gas analyzer (Gasboard 3100) was used to monitor the gas composition of the exhaust. The activity and stability of iron-based redox catalysts were investigated under 20 H<sub>2</sub>-CO<sub>2</sub> cycles at 650 °C. The sample was reduced under 10 vol% H<sub>2</sub>/N<sub>2</sub> (500 mL·min<sup>-1</sup>) for 10 min and followed an oxidation step by switching the gas to 50 vol % CO<sub>2</sub>/N<sub>2</sub> (500 mL·min<sup>-1</sup>) and keeping for 10 min. Between each reduction and oxidation half-cycles, pure N<sub>2</sub> was purged for 5 min. The reactivity is assessed by instantaneous CO space-time yield ( $STY_{CO}$ , mol<sub>CO</sub>·s<sup>-1</sup>·kg<sub>Fe<sub>2</sub>O<sub>3</sub></sub><sup>-1</sup>).

$$STY_{CO} = \frac{|F_{CO,0} - F_{CO}|}{m_i}$$

where,  $F_{CO,0}$  (mol·s<sup>-1</sup>) and  $F_{CO}$  (mol·s<sup>-1</sup>) are the CO molar flow rates at the inlet and outlet of the reactor, respectively.

To mimic the characteristic of chemical looping process, time-averaged CO space time yield ( $\overline{STY_{CO}}$ ) is adopted to evaluate the reactivity of iron-based redox catalysts by using a multi-tube reactor configuration simulation based on  $STY_{CO}$  under single-tube reactor experiment. This simulation is similar to the multi-column pressure swing adsorption (PSA) system configured with a series of reactors, where each reactor is operated in a cyclic reaction and regeneration way with a time delay between two consecutive reactors [41,42].  $\overline{STY_{CO}}$  (mol<sub>CO</sub>·s<sup>-1</sup>·kg<sub>Fe<sub>2</sub>O<sub>3</sub></sub><sup>-1</sup>) is formulated by adding up the contribution of each reactor and removing the number of reactors in the oxidation state.

$$\overline{STY_{CO}} = \frac{\sum_{n_{ox}} F_{CO}}{n_{ox} \bullet m_i}$$

where,  $F_{CO}$  (mol<sub>CO</sub>·s<sup>-1</sup>) is the molar flow rate of CO product at the outlet,  $m_i$  is the mass of Fe<sub>2</sub>O<sub>3</sub> in the reactor,  $n_{ox}$  is the number of reactors in

an oxidation state.

## 2.4. DFT calculations

The DFT calculations were spin-polarized and performed using the Perdew-Burke-Ernzerhof (PBE) [43] functional in the Vienna Ab initio Simulation Package (VASP) [44,45]. The D3 correction method [46] was used to account for van der Waals (vdW) interactions [47,48]. The project-augmented wave (PAW) method was used to represent the core-valence interaction. For the total energy calculations, a cut-off energy of 450 eV was set for plane-wave basis sets to expand the valence electronic states. The force on each relaxed atom was converged below 0.05 eV/Å for structural optimizations. For the transition metals Zr and Fe, DFT+U was applied where the on-site coulomb correction was set on Zr and Fe 3d orbitals with an effective U value of 4.0 eV, as suggested in other theoretical works [49,50]. The adsorption energy ( $\Delta G_{ad}$ ) was defined as:

$$\Delta G_{ad} = G_{adsorbate+surface} - G_{adsorbate} - G_{surface}$$

where  $G_{surface}$ ,  $G_{adsorbate}$ , and  $G_{adsorbate+surface}$  are the free energies of the surface, adsorbate in the gas phase, and adsorbate adsorbed on the surface, respectively. The free energy G is calculated from the total energy E (by DFT calculation) and thermal corrections (including zero-point energy ZPE, internal energy U, and entropy S):

$$G = E_{DFT} + ZPE + U - TS$$

All thermal corrections are obtained by frequency calculations of VASP followed by VASPKIT data processing [51]. The transition states (TS) were determined using a constrained optimization scheme [52,53] and verified until (i) all forces on atoms vanished and (ii) the total energy reached a maximum along the reaction coordinate but a minimum with respect to the rest of the degrees of freedom.

Two common zirconia surfaces, m-ZrO<sub>2</sub> (101) and t-ZrO<sub>2</sub> (001), were selected to begin DFT calculations (Fig. S1). The optimized lattices of bulk monoclinic ZrO<sub>2</sub> (a = 5.218, b = 5.280, c = 5.358 Å, β = 99.12°) and tetragonal ZrO<sub>2</sub> (a = b = 3.638, c = 5.174 Å) agree well with the experimental data (a = 5.145, b = 5.208, c = 5.311 Å, β = 99.23°) and (a = b = 3.644, c = 5.315 Å), demonstrating the reliability of the calculations.

## 3. Results and discussion

### 3.1. The type and intensity of oxide/metal-support interaction between ZrO<sub>2</sub> and FeO<sub>x</sub>

The type and intensity of the interaction between Fe<sub>2</sub>O<sub>3</sub> and ZrO<sub>2</sub> with two crystalline phases (m-ZrO<sub>2</sub> and t-ZrO<sub>2</sub>) are firstly determined by DFT calculations (Fig. 1, S1 and S2), XPS detection (Fig. S3) and H<sub>2</sub>-TPR (Fig. S4). The Fe<sub>2</sub>O<sub>3</sub>-ZrO<sub>2</sub> models using Fe<sub>4</sub>O<sub>6</sub> clusters supported on crystalline phases are constructed to illuminate the difference on structural and electronic properties (Figs. 1, S1 and S2). Compared to Fe<sub>2</sub>O<sub>3</sub>/t-ZrO<sub>2</sub>, Fe<sub>2</sub>O<sub>3</sub>/m-ZrO<sub>2</sub> exhibits a lower binding energy and a larger bond length (Fig. 1a-b and Table S1), indicating a lower stability than the former material [30]. Moreover, from Barder charge analysis (Fig. S2), doping Fe into m-ZrO<sub>2</sub> enriches more electrons (0.02 e<sup>-</sup>) than that into t-ZrO<sub>2</sub>. This implies that the interaction between ZrO<sub>2</sub> and Fe<sub>2</sub>O<sub>3</sub> is electronic transfer. When Fe<sub>2</sub>O<sub>3</sub> cluster is supported on ZrO<sub>2</sub> (Fig. 1c-d), m-ZrO<sub>2</sub> tends to transfer more electrons (0.04 e<sup>-</sup>) than t-ZrO<sub>2</sub>, implying that Fe<sub>2</sub>O<sub>3</sub>/m-ZrO<sub>2</sub> shows a stronger intensity of electronic oxide-support interaction than Fe<sub>2</sub>O<sub>3</sub>/t-ZrO<sub>2</sub>.

The electronic interaction intensity between ZrO<sub>2</sub> and iron oxide is furtherly confirmed by XPS detection and H<sub>2</sub>-TPR of the as-synthesized samples (Figs. S3 and S4). From Fig. S3a, the peaks at 710.3–710.6 eV and 723.6–723.9 eV belong to Fe 2p<sub>3/2</sub> and Fe 2p<sub>1/2</sub>, respectively, and the peak at 718 eV is a satellite peak [54], which is consistent with the

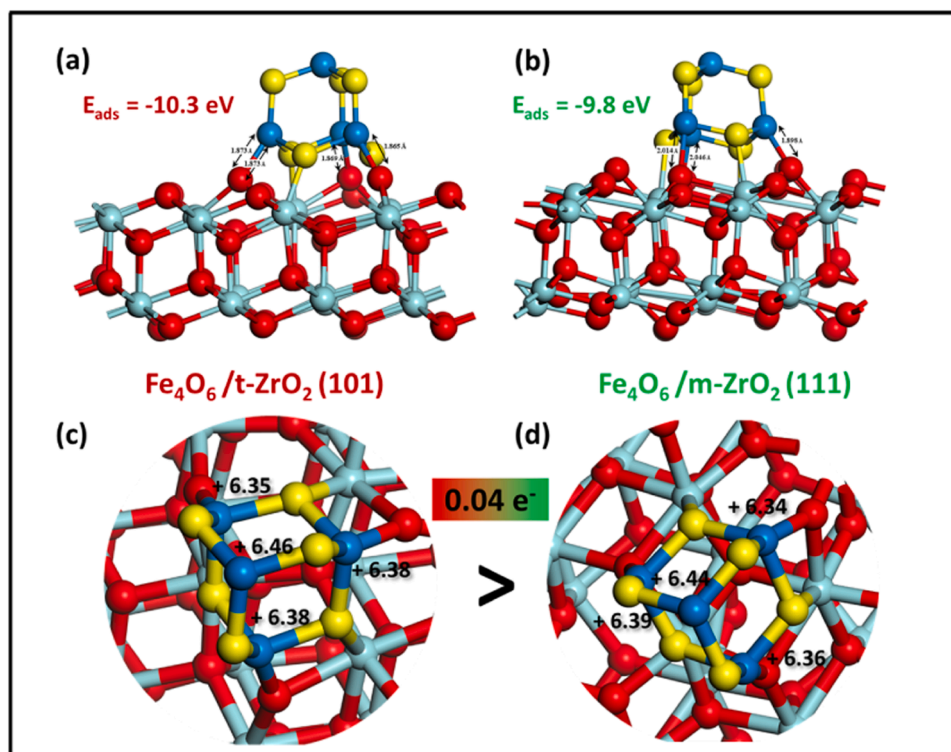


Fig. 1. The structural and electronic properties of  $\text{Fe}_4\text{O}_6$  clusters supported on two  $\text{ZrO}_2$  crystalline phases: (a, b) binding energy; (c, d) charge distribution.

characteristic peak of  $\text{Fe}_2\text{O}_3$  as observed in XRD (Fig. 2a). Compared with Fe 2p and Zr 3d spectrum of freshly  $\text{Fe}_2\text{O}_3/\text{ZrO}_2$  catalysts, the binding energy of Fe 2p<sub>3/2</sub> in  $\text{Fe}_2\text{O}_3/\text{m-ZrO}_2$  (710.3 eV) is lower than that of other samples. On the contrary, the binding energy of Zr 3d<sub>5/2</sub> in  $\text{Fe}_2\text{O}_3/\text{m-ZrO}_2$  (182.9 eV) is higher than that in  $\text{Fe}_2\text{O}_3/\text{t-ZrO}_2$  (182.8 eV). This demonstrates an electron transfer between iron oxide and zirconia, meanwhile, m- $\text{ZrO}_2$  shows a higher electron density than t- $\text{ZrO}_2$ . Fig. S4 illustrates the lowest reduction temperature for  $\text{Fe}_2\text{O}_3/\text{m-ZrO}_2$ , which is ascribed to that m- $\text{ZrO}_2$  is easier reduced at the interface between  $\text{Fe}_2\text{O}_3$  and m- $\text{ZrO}_2$  to induce a stronger oxide-support interaction for promoting the reduction of iron oxide. Moreover,  $\text{Fe}_2\text{O}_3/\text{m-ZrO}_2$  shows a larger peak for the last reduction step than other three  $\text{Fe}_2\text{O}_3/\text{ZrO}_2$  samples (Fig. S4), implying a stronger metal-support interaction between iron and m- $\text{ZrO}_2$ . The good agreement between calculation and characterization lays a good foundation to identify the influence of electronic interaction intensity on the redox reactivity and reaction mechanism.

### 3.2. Characterizations of as-calcined and cycled redox catalysts

The crystalline phases of  $\text{ZrO}_2$  supports, as-calcined and cycled catalysts are determined by XRD (Fig. 2a, b and S5). m- $\text{ZrO}_2$  (JCPD: 37-1484), t- $\text{ZrO}_2$  (JCPD: 49-1642) and their mixtures (noted as mix- $\text{ZrO}_2$ ) were successfully synthesized as their diffraction peaks are consistent with their standard cards (Fig. S5a). After loading iron, the characteristic peak of  $\text{Fe}_2\text{O}_3$  (JCPD: 33-0664) appears in the freshly materials. Compared to the diffraction peak positions of  $\text{ZrO}_2$ ,  $\text{Fe}_2\text{O}_3/\text{m-ZrO}_2$  and  $\text{Fe}_2\text{O}_3/\text{mix-ZrO}_2$  show a slight shift of  $\text{ZrO}_2$  angle to a high value but no such phenomenon is observed for  $\text{Fe}_2\text{O}_3/\text{t-ZrO}_2$  (Fig. S5b). This indicates that the addition of iron causes a lattice distortion of m- $\text{ZrO}_2$  to form Fe-O-Zr bonds since  $\text{Fe}^{3+}$  (74 Å) has a smaller ionic radius than  $\text{Zr}^{4+}$  (86 Å) [55,56]. The presence of Fe-O-Zr structure leads to a phase transition from t- $\text{ZrO}_2$  to m- $\text{ZrO}_2$  during redox cycles, confirming by an increase of m- $\text{ZrO}_2$  volume fraction in  $\text{Fe}_2\text{O}_3/\text{mix-ZrO}_2$  (Fig. S6). This is related to the nature of  $\text{ZrO}_2$  material that metal doping destroys the stabilization of high temperature polymorphs and causes a phase

transition under air calcination [57,58] or low oxygen concentration conditions [59,60]. In addition, the slight variation of crystallite size during cycles (Tables S2 and S3) means that  $\text{ZrO}_2$  favors a good stability for iron-based redox catalysts.

The surface area, pore volume and pore size of the materials are examined by  $\text{N}_2$  adsorption-desorption tests (Fig. S7 and Table S4). All the samples show an IV isothermal curve with large amounts of mesoporous (<10 nm, Fig. S7).  $\text{Fe}_2\text{O}_3/\text{t-ZrO}_2$  materials exhibit a larger specific surface area but a smaller pore size than  $\text{Fe}_2\text{O}_3/\text{m-ZrO}_2$  catalysts (Table S4), which illustrates that t- $\text{ZrO}_2$  is preferred to maintain a better structural stability under calcination than m- $\text{ZrO}_2$ . This is also confirmed by DFT calculation result that the binding energy between  $\text{Fe}_2\text{O}_3$  and t- $\text{ZrO}_2$  is larger than that and m- $\text{ZrO}_2$  (Fig. 1a). As determined by ICP-OES, the iron content is around 7 % for all the samples (Table S4) which is compatible to the theoretical value. From SEM (Fig. 2c and S8),  $\text{Fe}_2\text{O}_3/\text{m-ZrO}_2$  possesses a smaller particle than other two materials before and after cycles, even though a similar bulk morphology is found for  $\text{ZrO}_2$  with different crystalline phases. The almost unchanged microstructure during cycles indicates a good stability for these three catalysts, which is consistent with the variation of crystal size (Tables S2 and S3). As measured by XPS, the Fe/Zr ratio on the surface of iron-based redox catalysts is slightly greater than 2:3 (Table S5), implying the accumulation of  $\text{Fe}_2\text{O}_3$  on the surface of the catalysts. This furtherly confirms the accuracy of the established molecular model in DFT calculations using  $\text{Fe}_2\text{O}_3$  cluster at the surface of  $\text{ZrO}_2$  (Fig. S1). HRTEM illustrates the crystal planes of  $\text{ZrO}_2$  and  $\text{Fe}_2\text{O}_3$ , where  $d = 0.27$  nm,  $d = 0.29$  nm and  $d = 0.37$  nm are corresponded to m- $\text{ZrO}_2$  (111), t- $\text{ZrO}_2$  (111), and  $\text{Fe}_2\text{O}_3$  (012), respectively (Fig. 2d). This confirms the presence of crystalline phase and plane for the as-prepared redox catalysts.

### 3.3. Redox performance and thermal stability

The oxygen storage capacity, reduction rate and oxidation rate are examined to assess the redox ability of as-synthesized samples (Figs. 3a, b and S9). The m- $\text{ZrO}_2$  promoted samples possess larger oxygen storage capacity (Fig. S9a), reduction rate and oxidation rate than t- $\text{ZrO}_2$  and



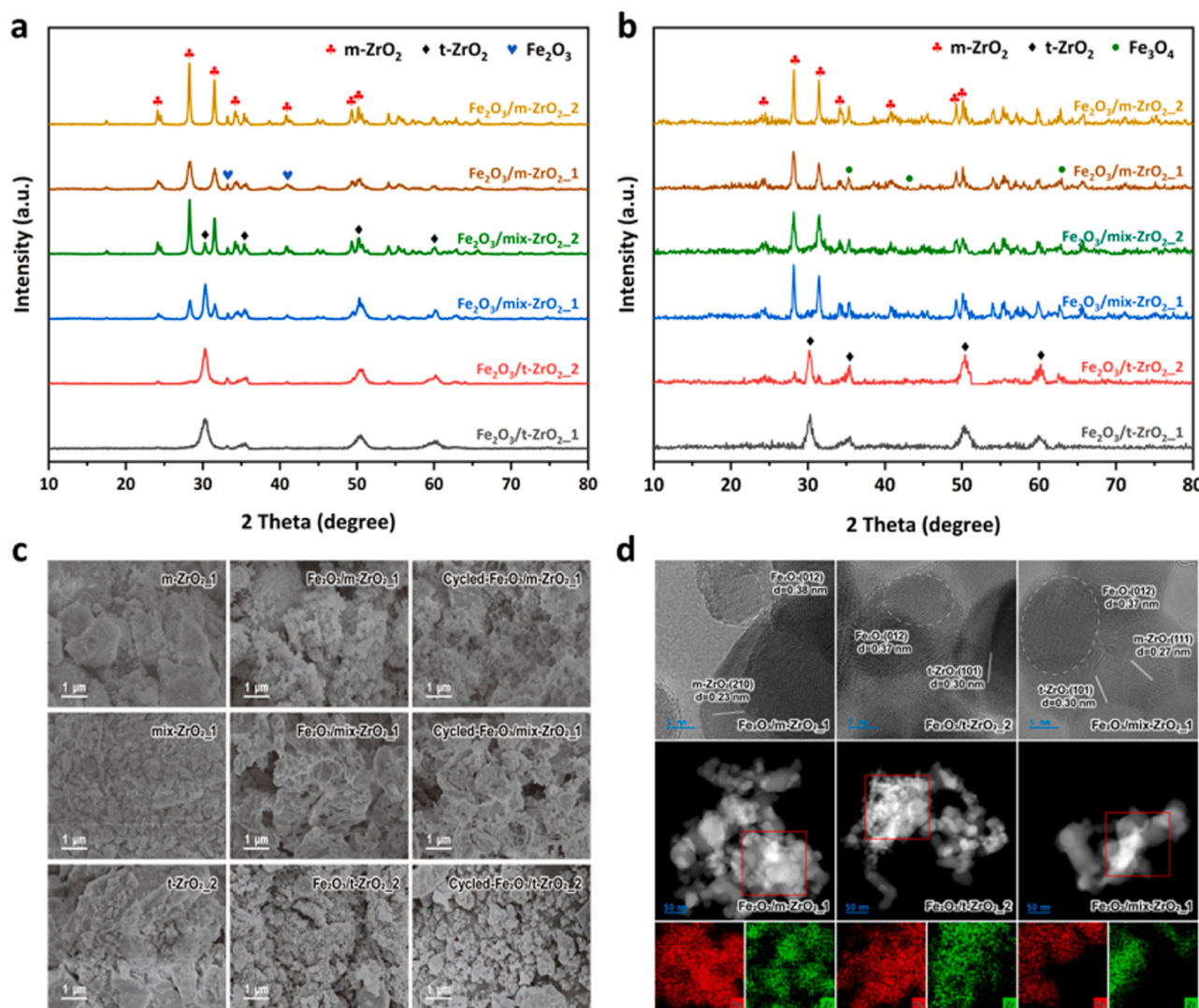


**Fig. 2.** The characterizations of iron-based redox catalysts: (a) XRD pattern of as-calcined samples, (b) XRD spectrum of cycled materials, (c) SEM images of as-prepared and cycled catalysts, and (d) HRTEM and EDS images of freshly samples.

mix- $\text{ZrO}_2$  supported materials. Especially by eliminating the impact of particle size (i.e. choosing  $\text{Fe}_2\text{O}_3/\text{m-ZrO}_2\text{-1}$ ,  $\text{Fe}_2\text{O}_3/\text{mix-ZrO}_2\text{-1}$  and  $\text{Fe}_2\text{O}_3/\text{t-ZrO}_2\text{-2}$  with almost identical crystal size, Table S2), a similar result is obtained that m- $\text{ZrO}_2$  presents an obvious enhancement on the redox ability than t- $\text{ZrO}_2$  (Figs. S9c,d). For instance,  $\text{Fe}_2\text{O}_3/\text{m-ZrO}_2\text{-1}$  gains the maximum reduction and oxidation rates of 2.23 and 5.03  $\text{mmol}_{[\text{O}]} \cdot (\text{s} \cdot \text{g}_{\text{Fe}_2\text{O}_3})^{-1}$ , which was 1.8 and 2.5 times that of  $\text{Fe}_2\text{O}_3/\text{t-ZrO}_2\text{-2}$  (1.20 and 2.00  $\text{mmol}_{[\text{O}]} \cdot (\text{s} \cdot \text{g}_{\text{Fe}_2\text{O}_3})^{-1}$ ), respectively. This is related to that the loose binding between  $\text{Fe}_2\text{O}_3$  and m- $\text{ZrO}_2$  (Fig. 1) is benefitted to improve the redox ability. In contrast, pure zirconia shows limited oxygen storage capacity ( $< 0.2\%$ ) (Fig. S9b), implying that two  $\text{ZrO}_2$  crystalline phases act as physical barriers to prevent the sintering of the catalysts.

The CO production activity and stability of iron-based redox catalysts with different  $\text{ZrO}_2$  crystalline phases were evaluated by twenty isothermal  $\text{H}_2\text{-CO}_2$  cycles with the evolution of time-averaged CO space-time yield ( $\overline{\text{STY}}_{\text{CO}}$ ) (Fig. 3c). Due to the self-activation effect [61–63], three catalysts perform with an increase of  $\overline{\text{STY}}_{\text{CO}}$  at the beginning cycles, which is related to the evolution of material structure (e.g. phase transition and porosity) during redox reactions.  $\text{Fe}_2\text{O}_3/\text{m-ZrO}_2\text{-1}$  shows the largest  $\overline{\text{STY}}_{\text{CO}}$ , even though a partial decline of CO production occurs with increasing cycles. Its  $\overline{\text{STY}}_{\text{CO}}$  can still reach 560  $\text{mmol}_{\text{CO}} \cdot \text{s}^{-1} \cdot \text{kg}_{\text{Fe}_2\text{O}_3}^{-1}$ ,

which is three times of that for  $\text{Fe}_2\text{O}_3/\text{t-ZrO}_2$ . This result implies the superiority of m- $\text{ZrO}_2$  with strong electronic interaction with iron oxide. With the progressing of cycles, the time-averaged  $\overline{\text{STY}}_{\text{CO}}$  of  $\text{Fe}_2\text{O}_3/\text{mix-ZrO}_2\text{-1}$  increases significantly from 376  $\text{mmol}_{\text{CO}} \cdot \text{s}^{-1} \cdot \text{kg}_{\text{Fe}_2\text{O}_3}^{-1}$  to 469  $\text{mmol}_{\text{CO}} \cdot \text{s}^{-1} \cdot \text{kg}_{\text{Fe}_2\text{O}_3}^{-1}$ . This is because the crystalline phases of zirconia in the sample are completely transformed into m- $\text{ZrO}_2$  after redox cycles (Fig. S6).

For the materials with the same  $\text{ZrO}_2$  crystalline phase, smaller  $\text{Fe}_2\text{O}_3/\text{Fe}_3\text{O}_4$  crystalline size (Tables S3 and S4) results in a higher activity (Fig. 3c). For instance,  $\text{Fe}_2\text{O}_3/\text{m-ZrO}_2\text{-1}$  (52.8 nm),  $\text{Fe}_2\text{O}_3/\text{t-ZrO}_2\text{-2}$  (28.3 nm) and  $\text{Fe}_2\text{O}_3/\text{mix-ZrO}_2\text{-1}$  (54.4 nm) show a better performance than  $\text{Fe}_2\text{O}_3/\text{m-ZrO}_2\text{-2}$  (58.3 nm),  $\text{Fe}_2\text{O}_3/\text{t-ZrO}_2\text{-1}$  (52.0 nm) and  $\text{Fe}_2\text{O}_3/\text{mix-ZrO}_2\text{-2}$  (71.3 nm), respectively. This is because small crystalline size is benefitted to decrease the activation energy for deriving the redox reaction and promote the migration of oxygen ions and electrons [64,65]. Under this condition,  $\text{ZrO}_2$  crystalline size leads to no effect on the activity. Compared to different  $\text{ZrO}_2$  crystalline phases, m- $\text{ZrO}_2$  supported catalysts always exhibit a more favorable activity than other the materials supported by other two  $\text{ZrO}_2$  phases (Fig. 3c), which is related to the stronger oxide-support interaction induced by m- $\text{ZrO}_2$  than by t- $\text{ZrO}_2$ . However, in terms of two  $\text{Fe}_2\text{O}_3/\text{m-ZrO}_2$  and two  $\text{Fe}_2\text{O}_3/\text{mix-ZrO}_2$  samples,  $\text{Fe}_2\text{O}_3/\text{m-ZrO}_2\text{-1}$  obtains a larger  $\overline{\text{STY}}_{\text{CO}}$  than other three materials, due to the smaller

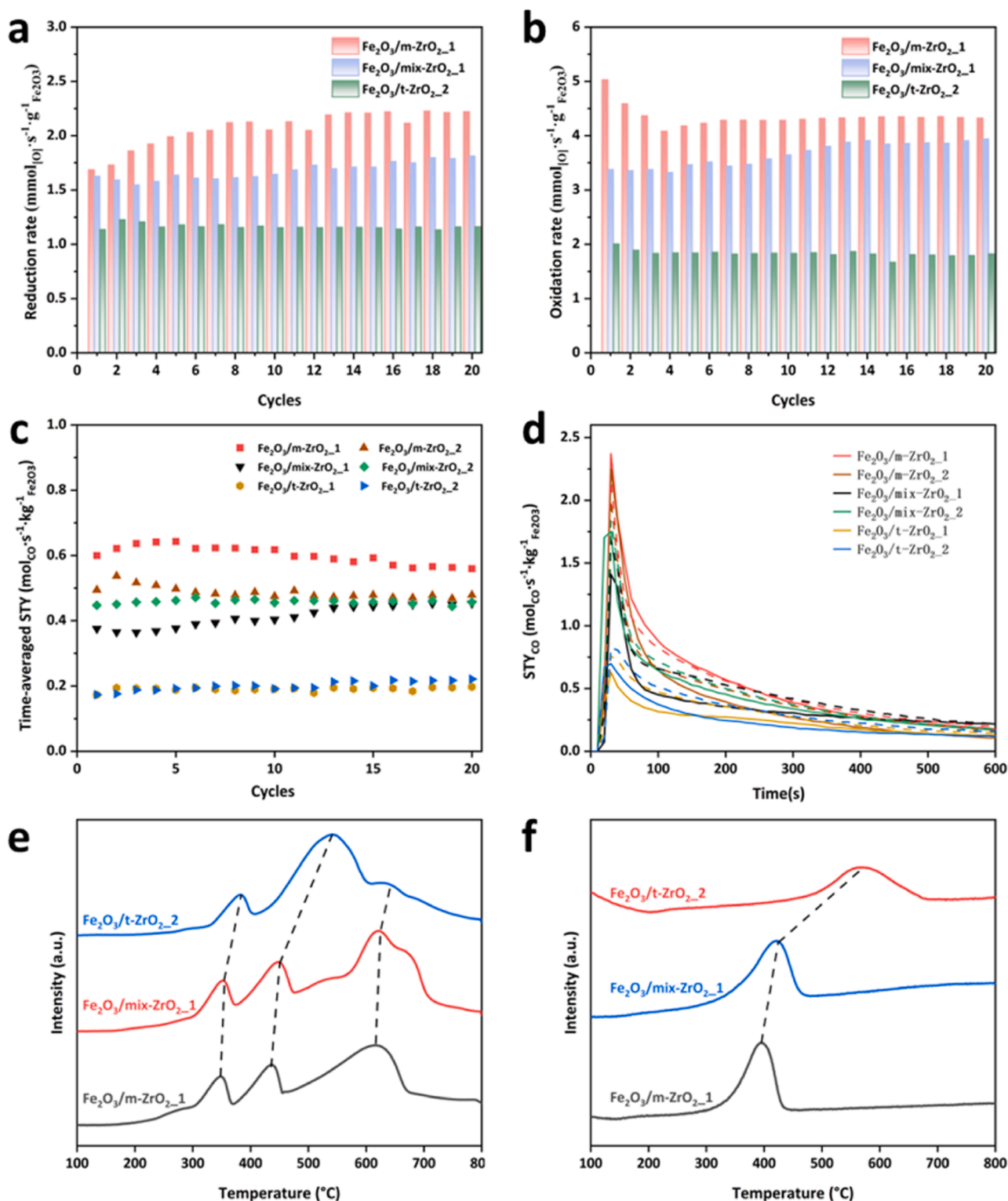


**Fig. 3.** The (a) reduction rate and (b) oxidation rate of iron-based redox catalysts, the reactivity of iron-based redox catalysts with different ZrO<sub>2</sub> crystalline phases: (c) time-averaged CO space time yield, (d) CO space-time yield at CO<sub>2</sub> re-oxidation half cycle, the solid and dash lines represent the first and 20th cycles, (e) H<sub>2</sub>-TPR and (f) CO<sub>2</sub>-TPO.

crystalline sizes for both iron oxide and support. Due to the interactions between iron oxide and ZrO<sub>2</sub> with different crystalline sizes, other three samples gain almost the same CO production after 20 redox cycles.

The instantaneous CO space time yield of iron-based redox catalysts during CO<sub>2</sub> re-oxidation half-cycles is compared (Figs. 3d and S10). A maximum value of STY<sub>CO</sub> is observed for Fe<sub>2</sub>O<sub>3</sub>/mix-ZrO<sub>2</sub> samples and

decreases with increasing t-ZrO<sub>2</sub> content. Limited reactivity deactivation is found for all the samples even with an increase of maximum STY<sub>CO</sub> at the beginning cycles, indicating two ZrO<sub>2</sub> crystals can both maintain a good stability for the catalysts. Moreover, the presence of different ZrO<sub>2</sub> crystalline phases contributes to a limited effect on the reaction time as all the samples show a similar reaction profile for CO

production (Figs. 3d and S10).

H<sub>2</sub>-TPR and CO<sub>2</sub>-TPO were carried out to confirm the H<sub>2</sub> and CO<sub>2</sub> activations by iron-based redox catalysts with different ZrO<sub>2</sub> crystal phases (Figs. 3e, f, S4, S11 and S12). Three reduction stages of iron oxide (Fe<sub>2</sub>O<sub>3</sub>→Fe<sub>3</sub>O<sub>4</sub>→FeO→Fe) and one oxidation stage (Fe→Fe<sub>3</sub>O<sub>4</sub>) are found for all the Fe<sub>2</sub>O<sub>3</sub>/ZrO<sub>2</sub> samples, which is the nature of iron-based redox catalysts [66]. The reduction and oxidation temperature are the lowest for Fe<sub>2</sub>O<sub>3</sub>/m-ZrO<sub>2</sub> and shift to a higher value as the increment of t-ZrO<sub>2</sub> content. For instance, the beginning temperature of reduction and oxidation varies from 360 °C and 390 °C to 380 °C and 570 °C when the crystal phase changes from m-ZrO<sub>2</sub> to t-ZrO<sub>2</sub>. This temperature shift indicates that m-ZrO<sub>2</sub> is beneficial for H<sub>2</sub> and CO<sub>2</sub> activations to make the reduction and oxidation of iron-based redox catalysts easier than t-ZrO<sub>2</sub>. The way of H<sub>2</sub> and CO<sub>2</sub> activations originate from the interface and oxide/metal-support interactions (Fig. S11). During H<sub>2</sub> reduction half-cycle, m-ZrO<sub>2</sub> is easier reduced at the interface between Fe<sub>2</sub>O<sub>3</sub> and m-ZrO<sub>2</sub> to form more oxygen vacancy than t-ZrO<sub>2</sub> (Fig. S12), which induces a stronger oxide-support interaction to facilitate the reduction of iron oxide with lower reduction temperature (Figs. 3c and S4). At the last H<sub>2</sub> reduction step, a larger H<sub>2</sub> consumption is observed for Fe<sub>2</sub>O<sub>3</sub>/m-ZrO<sub>2</sub> than Fe<sub>2</sub>O<sub>3</sub>/t-ZrO<sub>2</sub>. This indicates a stronger

metal-support interaction between Fe<sub>2</sub>O<sub>3</sub> and m-ZrO<sub>2</sub>, which results in a lower energy barrier for the step from linear adsorption to bending adsorption to enhance CO<sub>2</sub> activation during CO<sub>2</sub> re-oxidation half-cycle (Fig. S13). Moreover, this strong metal-support interaction favors the performance of CO<sub>2</sub> conversion to CO under varied re-oxidation conditions (5 %, 20 % and 50 % CO<sub>2</sub>; Fig. S14a and Table S6). Fe<sub>2</sub>O<sub>3</sub>/m-ZrO<sub>2</sub> shows a larger  $\overline{STY}_{CO}$  and  $\overline{STY}_{CO}$  than Fe<sub>2</sub>O<sub>3</sub>/t-ZrO<sub>2</sub> for all the CO<sub>2</sub> concentration cases, which is ascribed to that the stronger metal-support interaction between Fe<sub>2</sub>O<sub>3</sub> and m-ZrO<sub>2</sub> provides channel oxygen to facilitate the oxidation of metallic iron into more Fe<sub>3</sub>O<sub>4</sub> (Fig. S14b). The function of metal-support interaction for enhancing iron oxidation is similar to the case that Ni can be oxidized by CO<sub>2</sub> via the interface and metal-support interaction [67].

### 3.4. Correlation between electronic interaction intensity and redox activity

The relationship between electronic interaction intensity and CO production activity is revealed by XPS and DFT calculations (Figs. 4 and S15). After cycles, two peaks at 52.6–52.8 eV and 55.9–56.0 eV are observed for Fe3p (Fig. 4a), indicating the existence of Fe<sup>2+</sup> and Fe<sup>3+</sup>

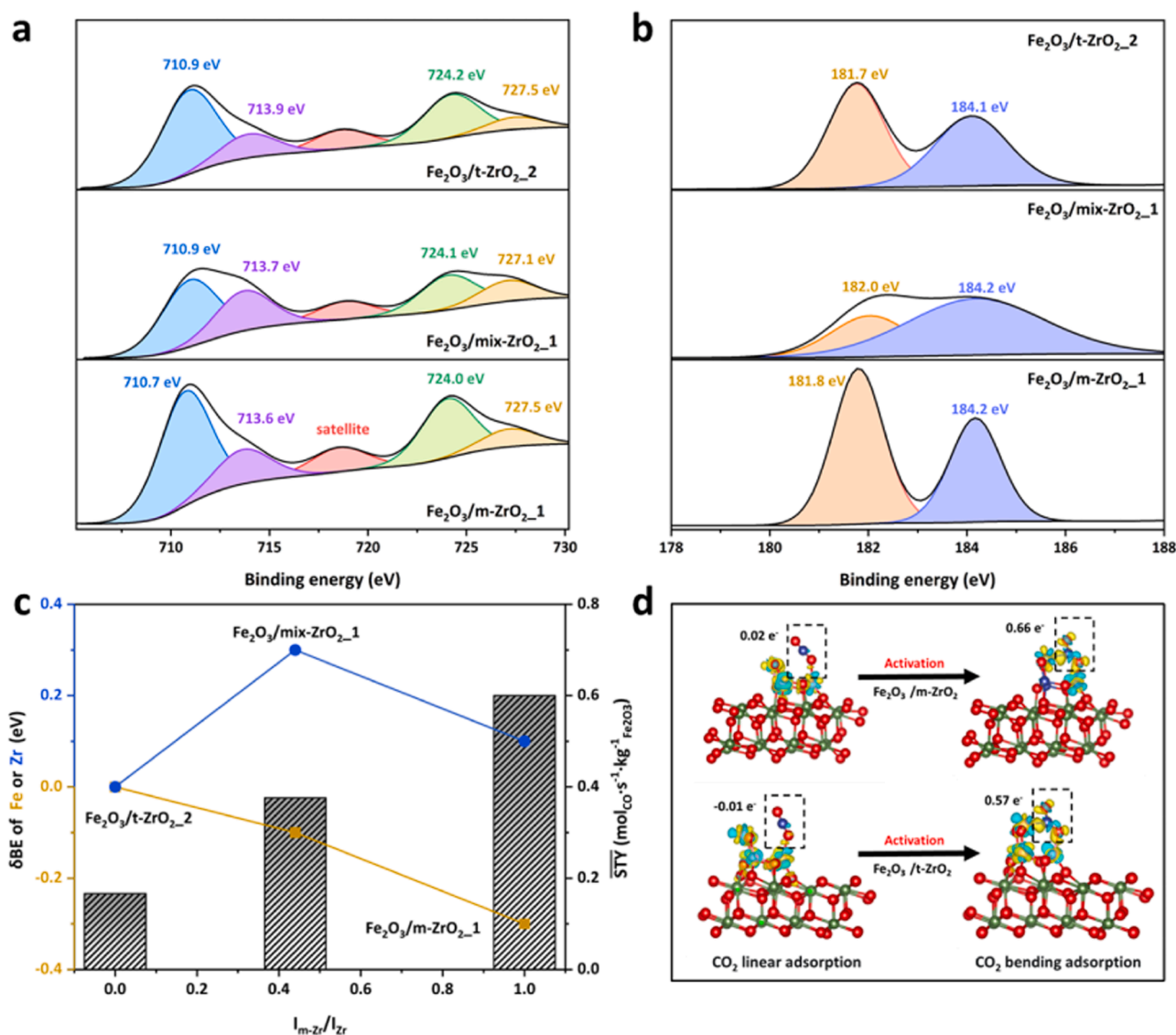


**Fig. 4.** The XPS spectrum of (a) Fe 2p and (b) Zr 3d; (c) time-averaged  $\overline{STY}_{CO}$  and binding energy (BE) shift of Fe 2p<sub>3/2</sub> (yellow) and Zr 3d<sub>5/2</sub> (blue) among catalysts in the initial stage of the reaction as a function of  $I_{m-Zr}/I_{Zr}$  and the (d) charge density difference analysis of iron-based redox catalysts.



ions [54]. This proves that the formation of  $\text{Fe}_3\text{O}_4$  even though its XRD diffraction peak is not obvious and overlaid by  $\text{ZrO}_2$  (Fig. S3).  $\text{Fe}_2\text{O}_3/\text{m-ZrO}_2$  shows a lower binding energy of Fe  $2p_{3/2}$  (710.7 eV) than other samples (Fig. 4a). In contrast, the binding energy of Zr  $3d_{5/2}$  in  $\text{Fe}_2\text{O}_3/\text{m-ZrO}_2$  (181.8 eV) is higher than that in  $\text{Fe}_2\text{O}_3/\text{t-ZrO}_2$  (181.7 eV, Fig. 4b). This binding energy shift of  $\text{Fe}2p_{3/2}$  and  $\text{Zr}3d_{5/2}$  implies that  $\text{Fe}_2\text{O}_3$  supported on m- $\text{ZrO}_2$  has a higher electron density than that on t- $\text{ZrO}_2$ . As the stronger electronegativity of  $\text{Fe}^{3+}$  compared to  $\text{Zr}^{4+}$ , the formation of Fe-O-Zr bonds leads to an increase and a decrease in the effective positive charge of Zr and Fe atoms, respectively. The correlation between electronic interaction intensity and time-averaged  $STY_{\text{CO}}$  as a function of  $I_{\text{m-Zr}}/I_{\text{Zr}}$  (the volume fraction of m- $\text{ZrO}_2$  in the  $\text{ZrO}_2$  support) is identified (Fig. 4c). The binding energy of Zr increases while that of Fe shifts to lower value with increasing  $I_{\text{m-Zr}}/I_{\text{Zr}}$ , suggesting that stronger electronic interaction between m- $\text{ZrO}_2$  and  $\text{Fe}_2\text{O}_3$  contributes to more electrons accumulated on the Fe atoms of  $\text{Fe}_2\text{O}_3/\text{m-ZrO}_2$  than that of  $\text{Fe}_2\text{O}_3/\text{t-ZrO}_2$ . The time-averaged  $STY_{\text{CO}}$  increases with increasing electronic interaction intensity, indicating that electron-rich  $\text{Fe}_2\text{O}_3$  is more conducive to  $\text{CO}_2$  reduction reaction.

Charge density difference analysis was furtherly applied to confirm the electron transfer between  $\text{Fe}_2\text{O}_3$  and  $\text{ZrO}_2$  during redox reaction (Fig. 4d and Table S7). During  $\text{H}_2$  reduction half-cycle (Table S7),  $^*\text{H}_2$  loses more electrons on the  $\text{Fe}_2\text{O}_3/\text{m-ZrO}_2$  (1.26  $e^-$ ) than that on  $\text{Fe}_2\text{O}_3/\text{t-ZrO}_2$  (-1.24  $e^-$ ). At  $\text{CO}_2$  re-oxidation stage, almost no electron transfer between the adsorbed molecule and  $\text{Fe}_2\text{O}_3/\text{ZrO}_2$  models occurs for  $\text{CO}_2$  linear adsorption. In contrast,  $\text{CO}_2$  molecules activated on  $\text{Fe}_2\text{O}_3/\text{m-ZrO}_2$  can accumulate more electrons (0.66  $e^-$ ) compared to  $\text{Fe}_2\text{O}_3/\text{t-ZrO}_2$  (0.56  $e^-$ ). Consistent to XPS and  $\text{H}_2$ -TPR results, this means the presence of strong electronic oxide-support interaction.

### 3.5. The effect of electronic interaction intensity on redox reaction mechanism

The influence of electronic interaction intensity on reaction mechanism was investigated (Fig. 5). During  $\text{H}_2$  reduction half-cycle (Fig. 5a), almost no energy barrier (< 0.1 eV) is required for the first step, since  $\text{H}_2$  is easily dissociated on the surface of transition metals [68]. Then, two H radicals on the  $\text{Fe}_2\text{O}_3$  surface are dissociated from the adsorbed  $\text{H}_2$  and combined with oxygen sites on metal clusters to form  $^*\text{H}_2\text{O}$ . For  $\text{Fe}_2\text{O}_3/\text{m-ZrO}_2$ , it needs overcoming an energy barrier of 0.65 eV, which is lower than that of  $\text{Fe}_2\text{O}_3/\text{t-ZrO}_2$  (0.93 eV). Afterward, the adsorbed  $^*\text{H}_2\text{O}$  dissociates as water molecule and flies away from metal cluster to form an oxygen vacancy.

During  $\text{CO}_2$  re-oxidation half-cycle (Fig. 5b),  $\text{CO}_2$  molecule is firstly

adsorbed at the deoxygenated sites of  $\text{Fe}_4\text{O}_6$  clusters in a linear manner.  $\text{Fe}_2\text{O}_3/\text{m-ZrO}_2$  releases 0.61 eV of heat to complete this free  $\text{CO}_2$  adsorption, which is slightly higher than that occurs on  $\text{Fe}_2\text{O}_3/\text{t-ZrO}_2$  (0.57 eV). As the linear adsorption is activated into bending adsorption (Fig. S13),  $^*\text{CO}_2$  absorbs 0.42 eV of heat on  $\text{Fe}_2\text{O}_3/\text{m-ZrO}_2$ , which is lower than that on  $\text{Fe}_2\text{O}_3/\text{t-ZrO}_2$  (0.97 eV). After that, for  $\text{Fe}_2\text{O}_3/\text{t-ZrO}_2$ , 2.00 eV of energy barrier is required to remove an oxygen atom from the activated  $^*\text{CO}_2$  and generate CO product. In contrast,  $\text{CO}_2$  re-oxidation is more easily achieved on  $\text{Fe}_4\text{O}_6$  clusters loaded on m- $\text{ZrO}_2$ , as the energy barrier is 1.56 eV.

This evolution of microscopic reaction steps during redox reactions means that the electronic interaction intensity leads to no effect on reaction mechanism, even though electron transfer appears both in freshly catalyst and during redox reactions. Due to the demand of a maximum energy barrier,  $\text{CO}_2$  re-oxidation is determined as the rate-determining step for iron-based catalysts with different electronic interaction intensities during redox reactions. In contrast, strong electronic oxide-support interaction is responsible for low reaction energy barriers, resulting in highly efficient chemical looping  $\text{CO}_2$  conversion to CO.

## 4. Conclusion

A crystal engineering strategy is proposed and examined to tune the intensity of electronic interaction between zirconia and iron oxide over iron-based redox catalysts for highly efficient chemical looping  $\text{CO}_2$  conversion to CO. CO yield shows a positive correlation with the intensity of electronic oxide/metal-support interaction. Compared to  $\text{Fe}_2\text{O}_3/\text{t-ZrO}_2$ ,  $\text{Fe}_2\text{O}_3/\text{m-ZrO}_2$  performs 1.8, 2.5 and 3 times of reduction rate, oxidation rate and time-averaged  $STY_{\text{CO}}$ . This is related to the role of  $\text{ZrO}_2$  played during redox cycles: (i) m- $\text{ZrO}_2$  shows a stronger electronic oxide-support interaction with iron oxide than t- $\text{ZrO}_2$ , which forms more oxygen vacancies at the interface to enhance  $\text{H}_2$  adsorption and facilitate the reduction of iron oxide; (ii) a stronger metal-support interaction between m- $\text{ZrO}_2$  and iron provides channel oxygen to promote the oxidation of metallic iron; (iii) stronger electronic transfer from m- $\text{ZrO}_2$  to  $\text{Fe}_2\text{O}_3$  occurs, which is more conducive to the activation of  $^*\text{CO}_2$  on the catalyst surface; (iv) the existence of m- $\text{ZrO}_2$  with high electronic interaction intensity decreases the energy barriers during redox reactions. This work opens a new window to develop efficient redox catalysts by regulating the crystalline structure and intensifying the composition interactions for thermochemical energy conversion and chemical looping applications.

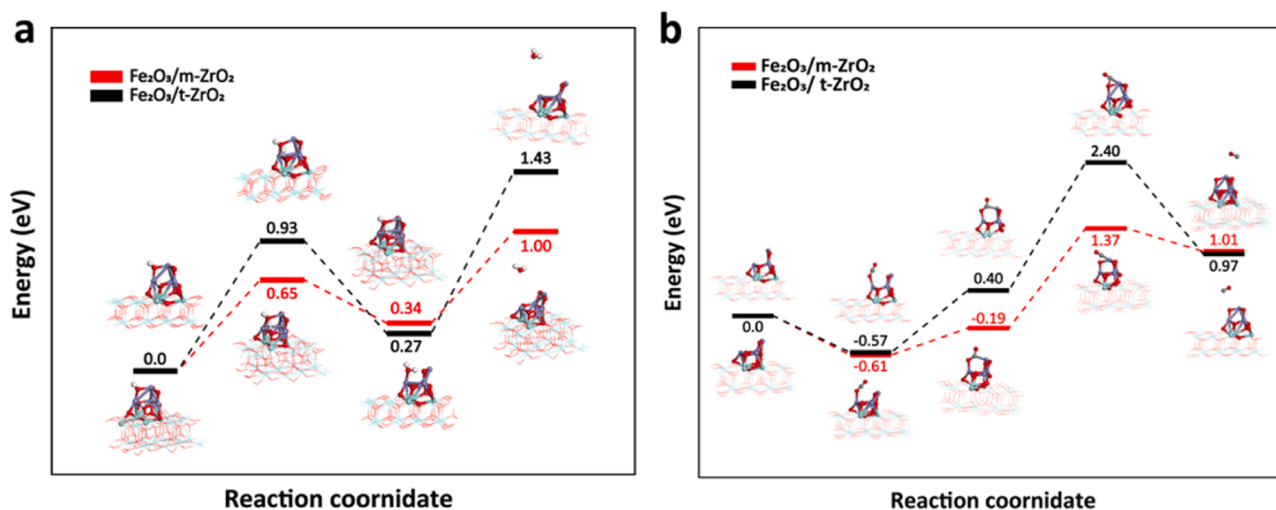


Fig. 5. The reaction mechanism for iron-based catalysts with two  $\text{ZrO}_2$  crystalline phases during  $\text{H}_2$ - $\text{CO}_2$  redox reactions: (a) energy profiles of each reaction steps during  $\text{H}_2$  reduction half-cycle; (b) energy profiles of each reaction steps during  $\text{CO}_2$  re-oxidation half-cycle.



## CRediT authorship contribution statement

**Tong Ouyang:** Formal analysis, Investigation, Writing – original draft. **Bo Jin:** Conceptualization, Funding acquisition, Methodology, Supervision, Writing – original draft, Writing – review & editing. **Yu Mao:** Methodology, Software, Writing – original draft. **Ding Wei:** Visualization, Writing – original draft. **Zhiwu Liang:** Funding acquisition, Resources, Writing – review & editing.

## Declaration of Competing Interest

The authors declare that they have no known competing financial interests or personal relationships that could have appeared to influence the work reported in this paper.

## Data availability

Data will be made available on request.

## Acknowledgements

The authors gratefully acknowledge the financial support from the National Natural Science Foundation of China (Grants U23A20118, 21808050 and 22138002), Key Projects of Hunan Provincial Department of Education (Grant 22A0015) and Fundamental Research Funds for the Central Universities (Grant 531107050907).

## Appendix A. Supporting information

Supplementary data associated with this article can be found in the online version at [doi:10.1016/j.apcatb.2023.123531](https://doi.org/10.1016/j.apcatb.2023.123531).

## References

- H.D. Matthews, S. Wynes, Current global efforts are insufficient to limit warming to 1.5°C, *Science* 376 (2022) 1404–1409.
- P. Voosen, Global temperatures in 2020 tied record highs, *Am. Assoc. Adv. Sci.* (2021).
- G.T. Rochelle, Amine scrubbing for CO<sub>2</sub> capture, *Science* 325 (2009) 1652–1654.
- W. Gao, S. Liang, R. Wang, Q. Jiang, Y. Zhang, Q. Zheng, B. Xie, C.Y. Toe, X. Zhu, J. Wang, L. Huang, Y. Gao, Z. Wang, C. Jo, Q. Wang, L. Wang, Y. Liu, B. Louis, J. Scott, A.-C. Roger, R. Amal, H. He, S.-E. Park, Industrial carbon dioxide capture and utilization: state of the art and future challenges, *Chem. Soc. Rev.* 49 (2020) 8584–8686.
- M.M. Hossain, H.I. de Lasa, Chemical-looping combustion (CLC) for inherent CO<sub>2</sub> separations—a review, *Chem. Eng. Sci.* 63 (2008) 4433–4451.
- L. Zeng, Z. Cheng, J.A. Fan, L.-S. Fan, J. Gong, Metal oxide redox chemistry for chemical looping processes, *Nat. Rev. Chem.* 2 (2018) 349–364.
- X. Zhu, Q. Imtiaz, F. Donat, C.R. Müller, F. Li, Chemical looping beyond combustion—a perspective, *Energy Environ. Sci.* 13 (2020) 772–804.
- J. Hu, V.V. Galvita, H. Poelman, G.B. Marin, Advanced chemical looping materials for CO<sub>2</sub> utilization: a review, *Materials* 11 (2018) 1187.
- Y. Liu, L. Qin, Z. Cheng, J.W. Goetze, F. Kong, J.A. Fan, L.-S. Fan, Near 100% CO selectivity in nanoscaled iron-based oxygen carriers for chemical looping methane partial oxidation, *Nat. Commun.* 10 (2019) 5503.
- J. Hu, H. Poelman, G.B. Marin, C. Detavernier, S. Kawi, V.V. Galvita, FeO controls the sintering of iron-based oxygen carriers in chemical looping CO<sub>2</sub> conversion, *J. CO<sub>2</sub> Util.* 40 (2020), 101216.
- Z. Ma, Y. Lu, G. Liu, Enhanced cyclic redox reactivity of Fe<sub>2</sub>O<sub>3</sub>/Al<sub>2</sub>O<sub>3</sub> by Sr doping for Chemical-Looping combustion of solid fuels, *Fuel* 324 (2022), 124625.
- T.W. van Deelen, C. Hernández Mejía, K.P. de Jong, Control of metal-support interactions in heterogeneous catalysts to enhance activity and selectivity, *Nat. Catal.* 2 (2019) 955–970.
- C. Yang, C. Pei, R. Luo, S. Liu, Y. Wang, Z. Wang, Z.-J. Zhao, J. Gong, Strong electronic oxide-support interaction over In<sub>2</sub>O<sub>3</sub>/ZrO<sub>2</sub> for highly selective CO<sub>2</sub> hydrogenation to methanol, *J. Am. Chem. Soc.* 142 (2020) 19523–19531.
- H. Tang, Y. Su, B. Zhang, A.F. Lee, M.A. Isaacs, K. Wilson, L. Li, Y. Ren, J. Huang, M. Haruta, Classical strong metal-support interactions between gold nanoparticles and titanium dioxide, *Sci. Adv.* 3 (2017), e1700231.
- N. Daelman, M. Capdevila-Cortada, N. López, Dynamic charge and oxidation state of Pt/CeO<sub>2</sub> single-atom catalysts, *Nat. Mater.* 18 (2019) 1215–1221.
- M.G. Willinger, W. Zhang, O. Bondarchuk, S. Shaikhutdinov, H.J. Freund, R. Schlögl, A case of strong metal-support interactions: combining advanced microscopy and model systems to elucidate the atomic structure of interfaces, *Angew. Chem. Int. Ed.* 53 (2014) 5998–6001.
- Z. Luo, G. Zhao, H. Pan, W. Sun, Strong metal-support interaction in heterogeneous catalysts, *Adv. Energy Mater.* 12 (2022) 2201395.
- W. Liu, J.S. Dennis, S.A. Scott, The effect of addition of ZrO<sub>2</sub> to Fe<sub>2</sub>O<sub>3</sub> for hydrogen production by chemical looping, *Ind. Eng. Chem. Res.* 51 (2012) 16597–16609.
- M.H. Jeong, J. Sun, G.Y. Han, D.H. Lee, J.W. Bae, Successive reduction-oxidation activity of FeO<sub>x</sub>/TiO<sub>2</sub> for dehydrogenation of ethane and subsequent CO<sub>2</sub> activation, *Appl. Catal. B Environ.* 270 (2020), 118887.
- F. Li, S. Luo, Z. Sun, X. Bao, L.-S. Fan, Role of metal oxide support in redox reactions of iron oxide for chemical looping applications: experiments and density functional theory calculations, *Energy Environ. Sci.* 4 (2011) 3661–3667.
- F. Li, Z. Sun, S. Luo, L.-S. Fan, Ionic diffusion in the oxidation of iron—effect of support and its implications to chemical looping applications, *Energy Environ. Sci.* 4 (2011) 876–880.
- L. Qin, M. Guo, Y. Liu, Z. Cheng, J.A. Fan, L.-S. Fan, Enhanced methane conversion in chemical looping partial oxidation systems using a copper doping modification, *Appl. Catal. B Environ.* 235 (2018) 143–149.
- G. Li, W. Yao, Y. Zhao, B. Jin, J. Xu, Y. Mao, X. Luo, Z. Liang, Reduction kinetics and carbon deposit for Cu-doped Fe-based oxygen carriers: role of Cu, *Chem. Eng. Sci.* 250 (2022), 117406.
- Y. Fan, B. Jin, Q. Guo, Z. Liang, Crystallite phase effect on the redox reactivity of layered double hydroxide-derived iron-based oxygen carriers for chemical looping CO<sub>2</sub> reduction, *ACS Sustain. Chem. Eng.* 11 (2023) 5999–6010.
- M. High, C.F. Patzschke, L. Zheng, D. Zeng, O. Gavalda-Diaz, N. Ding, K.H. H. Chien, Z. Zhang, G.E. Wilson, A.V. Berenov, Precursor engineering of hydrotalcite-derived redox sorbents for reversible and stable thermochemical oxygen storage, *Nat. Commun.* 13 (2022) 5109.
- M.M. Hossain, K.E. Sedor, H.I. De Lasa, Co-Ni/Al<sub>2</sub>O<sub>3</sub> oxygen carrier for fluidized bed chemical-looping combustion: desorption kinetics and metal-support interaction, *Chem. Eng. Sci.* 62 (2007) 5464–5472.
- M.M. Hossain, M.R. Quddus, H.I. De Lasa, Reduction kinetics of La modified NiO/La-γ-Al<sub>2</sub>O<sub>3</sub> oxygen carrier for chemical-looping combustion, *Ind. Eng. Chem. Res.* 49 (2010) 11009–11017.
- M.M. Hossain, D. Lopez, J. Herrera, H.I. de Lasa, Nickel on lanthanum-modified γ-Al<sub>2</sub>O<sub>3</sub> oxygen carrier for CLC: reactivity and stability, *Catal. Today* 143 (2009) 179–186.
- Y. Han, M. Tian, C. Wang, Y. Kang, L. Kang, Y. Su, C. Huang, T. Zong, J. Lin, B. Hou, Highly active and anticoke Ni/CeO<sub>2</sub> with ultralow Ni loading in chemical looping dry reforming via the strong metal-support interaction, *ACS Sustain. Chem. Eng.* 9 (2021) 17276–17288.
- H. Zhao, Y. Zhang, Y. Wei, J. Gui, Understanding CuO-support interaction in Cu-based oxygen carriers at a microcosmic level, *Proc. Combust. Inst.* 36 (2017) 4069–4077.
- Y. Zhao, B. Jin, Z. Zhang, K. Huang, Y. Wang, X. Luo, Q. Guo, Z. Liang, Tuning metal oxide-support interaction and crystal structure of prussian blue derived iron-based oxygen carriers for enhanced chemical looping CO<sub>2</sub> conversion, *Sep. Purif. Technol.* 310 (2023), 123089.
- W. Qin, Y. Wang, C. Dong, J. Zhang, Q. Chen, Y. Yang, The synergetic effect of metal oxide support on Fe<sub>2</sub>O<sub>3</sub> for chemical looping combustion: a theoretical study, *Appl. Surf. Sci.* 282 (2013) 718–723.
- M. Tian, C. Wang, L. Li, X. Wang, High performance of la-promoted Fe<sub>2</sub>O<sub>3</sub>/α-Al<sub>2</sub>O<sub>3</sub> oxygen carrier for chemical looping combustion, *AlChE J.* 63 (2017) 2827–2838.
- N.S. Yüzbaşı, A. Armutlulu, T. Huthwelker, P.M. Abdala, C.R. Müller, Na-β-Al<sub>2</sub>O<sub>3</sub> stabilized Fe<sub>2</sub>O<sub>3</sub> oxygen carriers for chemical looping water splitting: correlating structure with redox stability, *J. Mater. Chem. A* 10 (2022) 10692–10700.
- Y. Kang, M. Tian, Y. Wang, Y. Wang, C. Huang, Y. Zhu, L. Li, G. Wang, X. Wang, Silica modified alumina as supports of Fe<sub>2</sub>O<sub>3</sub> with high performance in chemical looping combustion of methane, *ACS Sustain. Chem. Eng.* 6 (2018) 12884–12892.
- J. Zhou, Z. Gao, G. Xiang, T. Zhai, Z. Liu, W. Zhao, X. Liang, L. Wang, Interfacial compatibility critically controls Ru/TiO<sub>2</sub> metal-support interaction modes in CO<sub>2</sub> hydrogenation, *Nat. Commun.* 13 (2022) 327.
- B. Jin, H. Poelman, C. Detavernier, Z. Liang, G.B. Marin, V.V. Galvita, Microstructured ZrO<sub>2</sub> coating of iron oxide for enhanced CO<sub>2</sub> conversion, *Appl. Catal. B Environ.* 292 (2021), 120194.
- F. Blaschke, M. Bele, B. Bitschnau, V. Hacker, The effect of microscopic phenomena on the performance of iron-based oxygen carriers of chemical looping hydrogen production, *Appl. Catal. B Environ.* 327 (2023), 122434.
- J. Huang, S. Jiang, M. Wang, X. Wang, J. Gao, C. Song, Dynamic evolution of Fe and carbon species over different ZrO<sub>2</sub> supports during CO prereduction and their effects on CO<sub>2</sub> hydrogenation to light olefins, *ACS Sustain. Chem. Eng.* 9 (2021) 7891–7903.
- T. Otroshchenko, O. Bulavchenko, H.V. Thanh, J. Rabeah, U. Bentrup, A. Matvienko, U. Rodemerck, B. Paul, R. Kraehnert, D. Linke, Controlling activity and selectivity of bare ZrO<sub>2</sub> in non-oxidative propane dehydrogenation, *Appl. Catal. A Gen.* 585 (2019), 117189.
- J. Hu, V.V. Galvita, H. Poelman, C. Detavernier, G.B. Marin, Catalyst-assisted chemical looping auto-thermal dry reforming: spatial structuring effects on process efficiency, *Appl. Catal. B Environ.* 231 (2018) 123–136.
- J. Hu, V.V. Galvita, H. Poelman, C. Detavernier, G.B. Marin, Pressure-induced deactivation of core-shell nanomaterials for catalyst-assisted chemical looping, *Appl. Catal. B Environ.* 247 (2019) 86–99.
- J.P. Perdew, K. Burke, M. Ernzerhof, Generalized gradient approximation made simple, *Phys. Rev. Lett.* 77 (1996) 3865.
- G. Kresse, J. Furthmüller, Efficiency of ab-initio total energy calculations for metals and semiconductors using a plane-wave basis set, *Comput. Mater. Sci.* 6 (1996) 15–50.

- [45] G. Kresse, J. Hafner, Ab initio molecular-dynamics simulation of the liquid-metal-amorphous-semiconductor transition in germanium, *Phys. Rev. B* 49 (1994) 14251.
- [46] J. Klimeš, D.R. Bowler, A. Michaelides, Van der Waals density functionals applied to solids, *Phys. Rev. B* 83 (2011), 195131.
- [47] G. Kresse, D. Joubert, From ultrasoft pseudopotentials to the projector augmented-wave method, *Phys. Rev. B* 59 (1999) 1758.
- [48] P.E. Blöchl, O. Jepsen, O.K. Andersen, Improved tetrahedron method for Brillouin-zone integrations, *Phys. Rev. B* 49 (1994) 16223.
- [49] V.I. Anisimov, F. Aryasetiawan, A.I. Lichtenstein, First-principles calculations of the electronic structure and spectra of strongly correlated systems: the LDA+ U method, *J. Phys. Condens. Matter* 9 (1997) 767.
- [50] S.L. Dudarev, G.A. Botton, S.Y. Savrasov, C.J. Humphreys, A.P. Sutton, Electron-energy-loss spectra and the structural stability of nickel oxide: an LSDA+ U study, *Phys. Rev. B* 57 (1998) 1505.
- [51] V. Wang, N. Xu, J.-C. Liu, G. Tang, W.-T. Geng, VASPKIT: a user-friendly interface facilitating high-throughput computing and analysis using VASP code, *Comput. Phys. Commun.* 267 (2021), 108033.
- [52] A. Alavi, P. Hu, T. Deutsch, P.L. Silvestrelli, J. Hutter, CO oxidation on Pt (111): an ab initio density functional theory study, *Phys. Rev. Lett.* 80 (1998) 3650.
- [53] Z.-P. Liu, P. Hu, General rules for predicting where a catalytic reaction should occur on metal surfaces: a density functional theory study of C–H and C–O bond breaking/making on flat, stepped, and kinked metal surfaces, *J. Am. Chem. Soc.* 125 (2003) 1958–1967.
- [54] T. Yamashita, P. Hayes, Analysis of XPS spectra of Fe<sup>2+</sup> and Fe<sup>3+</sup> ions in oxide materials, *Appl. Surf. Sci.* 254 (2008) 2441–2449.
- [55] L.J. France, W. Li, Y. Zhang, W. Mu, Z. Chen, J. Shi, Q. Zeng, X. Li, A superior Fe-Zr mixed oxide catalyst for the simultaneous reduction of NO and SO<sub>2</sub> with CO, *Appl. Catal. B Environ.* 269 (2020), 118822.
- [56] M. Behrens, S. Zander, P. Kurr, N. Jacobsen, Jr Senker, G. Koch, T. Ressler, R. W. Fischer, R. Schlögl, Performance improvement of nanocatalysts by promoter-induced defects in the support material: methanol synthesis over Cu/ZnO: Al, *J. Am. Chem. Soc.* 135 (2013) 6061–6068.
- [57] Y. Wu, J. Chen, W. Hu, K. Zhao, P. Qu, P. Shen, M. Zhao, L. Zhong, Y. Chen, Phase transformation and oxygen vacancies in Pd/ZrO<sub>2</sub> for complete methane oxidation under lean conditions, *J. Catal.* 377 (2019) 565–576.
- [58] F. Bi, X. Zhang, S. Xiang, Y. Wang, Effect of Pd loading on ZrO<sub>2</sub> support resulting from pyrolysis of UiO-66: application to CO oxidation, *J. Colloid Interface Sci.* 573 (2020) 11–20.
- [59] G. Stefanić, B. Grzeta, K. Nomura, R. Trojko, S. Musić, The influence of thermal treatment on phase development in ZrO<sub>2</sub>-Fe<sub>2</sub>O<sub>3</sub> and HfO<sub>2</sub>-Fe<sub>2</sub>O<sub>3</sub> systems, *J. Alloy. Compd.* 327 (2001) 151–160.
- [60] T.P. Otroshchenko, V.A. Kondratenko, U. Rodemerck, D. Linke, E.V. Kondratenko, Non-oxidative dehydrogenation of propane, n-butane, and isobutane over bulk ZrO<sub>2</sub>-based catalysts: effect of dopant on the active site and pathways of product formation, *Catal. Sci. Technol.* 7 (2017) 4499–4510.
- [61] T. Mattisson, A. Lyngfelt, P. Cho, The use of iron oxide as an oxygen carrier in chemical-looping combustion of methane with inherent separation of CO<sub>2</sub>, *Fuel* 80 (2001) 1953–1962.
- [62] S. Stendardo, L.K. Andersen, C. Herce, Self-activation and effect of regeneration conditions in CO<sub>2</sub>-carbonate looping with CaO–Ca<sub>12</sub>Al<sub>14</sub>O<sub>33</sub> sorbent, *Chem. Eng. J.* 220 (2013) 383–394.
- [63] J. Chen, L. Duan, F. Donat, C.R. Mueller, E.J. Anthony, M. Fan, Self-activated, nanostructured composite for improved CaL-CLC technology, *Chem. Eng. J.* 351 (2018) 1038–1046.
- [64] S. Liang, Y. Liao, W. Li, C. Li, X. Ma, Enhanced stability of iron-nickel oxygen carriers in biomass chemical looping gasification by core-shell structure, *Chem. Eng. J.* 451 (2023), 138964.
- [65] W. Akram, Sanjay, M.A. Hassan, Chemical looping combustion with nanosize oxygen carrier: a review, *Int. J. Environ. Sci. Technol.* 18 (2021) 787–798.
- [66] J. Zieliński, I. Zglinicka, L. Znak, Z. Kaszkur, Reduction of Fe<sub>2</sub>O<sub>3</sub> with hydrogen, *Appl. Catal. A Gen.* 381 (2010) 191–196.
- [67] V. De Coster, N.V. Srinath, P. Yazdani, H. Poelman, V.V. Galvita, Does CO<sub>2</sub> oxidize Ni catalysts? A quick x-ray absorption spectroscopy answer, *J. Phys. Chem. Lett.* 13 (2022) 7947–7952.
- [68] D.R. Aireddy, K. Ding, Heterolytic dissociation of H<sub>2</sub> in heterogeneous catalysis, *ACS Catal.* 12 (2022) 4707–4723.